OPEN ACCESS

Novel SoC-Based FBG Calibration Method for Decoupled Temperature and Strain Analysis within LIB Cells

To cite this article: Christopher Schwab *et al* 2024 *J. Electrochem. Soc.* **171** 110531
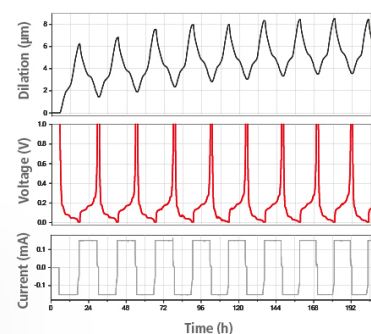
View the article online for updates and enhancements.

Novel SoC-Based FBG Calibration Method for Decoupled Temperature and Strain Analysis within LIB Cells

Christopher Schwab, Lea Leuthner,[z] and Anna Smith[z]

Karlsruhe Institute of Technology (KIT), Institute for Applied Materials (IAM), 76344 Eggenstein-Leopoldshafen, Germany

Internal temperature monitoring of battery cells can be very useful, as the core temperature can deviate significantly from that of the housing, especially in case of cells with a thick electrode stack. Conventional resistance temperature detectors can accurately measure temperature, but are limited to the outer surface of the cell due to induction effects. They are therefore not suitable for internal in situ measurements. Fiber Bragg grating (FBG) sensors are unaffected by the electric field as they operate by reflecting light. However, a specific difficulty is the distinction of temperature vs strain effects as the grating is sensitive to both. In this work a calibration routine to separate the influences of temperature and strain in a lithium-ion battery cell is presented and examined for two multi-layer stack pouch cells (10 and 20 Ah). The obtained in situ temperature data reveal a difference of up to 2 °C between center and cell housing at elevated discharge rate (4C) and a delay in detection of temperature peaks by the external sensor by 12 s. Strain data correlate with numbers of electrode layers in the stack and yield a stress of up to 27.3 MPa in the center of the 20 Ah cell.

As lithium-ion batteries (LIB) are present in almost all portable electronic devices and increasingly establish as first choice power storage system in vehicle electrification they have been subjected to immense variants of research.[1–5] The basic chemical and electrochemical characteristics were topic of numerous studies in the past. The objective now is to understand the influence factors affecting battery performance and life time[6] of which the impact of temperature is of particular importance.[7] If the optimum cell operating temperature window is not met, irreversible capacity loss,[8,9] decomposition of electrode materials, solid electrolyte interphase (SEI), and electrolyte that is associated with gas formation,[8–11] or Li plating[8,11–13] may occur, to name only a few effects. Also, a nonuniform temperature distribution inside a cell can negatively affect its lifetime, especially at higher C-rates.[14–18] Internal hotspots that are not detected by surface temperature measurements may result in permanent damage of the cell or even thermal runaway.[19] A precise acquisition and control of operating temperatures is thus required for a reliable battery management system and safe battery operation.[20–22] However, measuring the internal cell temperature without affecting the performance of a cell is not trivial. And even though there exist multiple different sensor approaches addressing the challenge of measuring internal temperatures ranging from direct to indirect methods, like thermocouples, thermally sensitive resistors or electrochemical impedance spectroscopy to name a few, they suffer from certain disadvantages, e.g. dependency on a reference temperature, susceptibility to corrosion, and noise.[23] Detailed overviews of various online internal temperature monitoring techniques were given by Jinasena et al.[24] and Huang et al.[22] and recently by Wang et al.[25]

The most promising measure technology is based on glass fibers with integrated fiber Bragg grating (FBG) sensors, which are heavily discussed in recent literature as a viable option for internal strain and temperature sensing technology.[20,22,24,26,27] They have been applied to various electrochemical systems such as aqueous batteries,[28] fuel cells,[29] LIB[30–37] and all-solid-state batteries (ASSB).[36] Furthermore, they were subject of many experiments for different cell types, ranging from Swagelok-type lab-cells to coin,[31,36,37] cylindrical[30,34,38] and pouch cells[32,33,35,39,40] up to cell pack level.[41–43] The advantages of FBG sensors are their outstanding properties of being inert towards most chemicals and the electric field within the cell. To further protect the fiber commonly polymer claddings are used, e.g., to avoid

dissolution of glass by traces of hydrofluoric acid found in typical LIB electrolytes.

However, FBG sensors are sensitive to both temperature changes and mechanical strain, as both parameters result in a distortion of the Bragg grating. The superposition effect represents a significant challenge when utilizing these sensors for temperature measurement in battery cells, given that temperature and strain vary simultaneously as a consequence of electrochemical changes and thermal expansion effects during the charging and discharging processes. In order to approach this problem multiple attempts have been made to differentiate between those two physical properties. For instance, the combination of two FBG sensors, one fixed onto the pouch cell using epoxy, so it is sensitive towards strain and temperature, and one loosely attached to solely react to temperature effects, leads to a reliable discrimination of both variables.[39,44,45] A similar setup was used by Ee et al. in combination with machine learning to establish a method to estimate the State of Charge (SoC) of a Li-ion cell.[46] Frazão et al. achieved simultaneous measurement of strain and temperature based on two Bragg gratings arranged in a twisted configuration.[47] Other measurements were conducted by Novais et al. on thin low-capacity pouch cells (20 mAh), where the temperature difference between the internal cell stack surface and external pouch bag surface of the cell was measured.[33] It was then assumed that strain influences are not measurable for the fact that these small cells are too thin to develop any strain, thus neglecting mechanical stress effects.[33] The significance of the location of FBG sensors has been shown by Bae et al. by integrating the sensor not only inside the cell but by comparing data of a FBG sensor placed on top of the anode coating with one that was directly integrated within the anode coating of the electrode.[48] Furthermore, a combination of FBG sensors with Fabry–Perot (FP) sensors, which are exclusively sensitive to strain, was presented. Using both sensors in immediate vicinity to each other, sole temperature data of the cell interior was obtained by subtracting the strain measured with the FP sensor from the FBG sensor signal.[32]

In this study, rather than setting up a complex measurement with multiple sensors, single fibers were placed within large-format multi-layer electrode stack Li-ion pouch cells based on $LiNi_{1/3}Mn_{1/3}Co_{1/3}O_2$ (NMC111) cathode and graphite anode material with capacities of 10 and 20 Ah and calibrated in a simplified approach towards temperature under constant SoC, as well as towards SoC under constant temperature. Applying this two-step calibration, temperature as well as strain-induced data was estimated separately for multiple FBG sensors contained within each fiber.

[z]E-mail: lea.leuthner@kit.edu; anna.smith@kit.edu

Then a rate performance test was applied to provide further insights into the thermal behavior of the cells. Two configurations for the positioning of the fiber were employed. The first was a relatively straightforward measurement setup, in which the position was located on top of the cell stack (10 Ah cell). The second was a more sophisticated setup, in which the fiber was situated in the center of the cell stack (20 Ah cell). This enabled an investigation of the thermal behavior as a function of both the stack thickness and the stack position. The results are discussed in comparison with data collected using a common external NTC5K temperature sensor placed on the surface of the cells.

Sensing Principle

FBGs have been part of research for a few decades now.[49,50] Figure 1a shows a schematic representation of the underlying measuring principle. By injecting light (λ_{in}) with a set range of wavelengths along the glass fiber core these sensors act as Bragg reflectors being capable of reflecting a certain base wavelength (λ_{ref}) at a grating with periodic change in the core's refractive index, with the remaining spectrum of light being transmitted (λ_t) (Eq. 1). These reflected wavelengths are then measured by an interrogator, which also provides the wavelength range for λ_{in}. This allows for using multiple FBG sensors within one glass fiber by using different λ_{ref} for each FBG sensor.

$$\lambda_{ref} = \lambda_{in} - \lambda_t \qquad [1]$$

The reflected wavelength is depending on the spacing of the sensor grating (Λ) and the effective refractive index of the fiber core (n_{eff}) (Eq. 2).

$$\lambda_{ref} = 2n_{eff}\Lambda \qquad [2]$$

As changes in temperature or application of mechanical strain (extensional along the fiber or orthogonally due to pressure onto the FBG sensor area) lead to deformation of the grating and thus

induce a change in its spacing, they directly affect the reflected wavelength. Whereas multiple fiber specific coefficients are normally used to calculate temperature or strain changes separately from each other, a recalibration is needed in case these fibers are inserted into LIB cells and are subjected to both parameters simultaneously.

An overview of nomenclatures of all variables used in this paper is given in Table I.

Experimental

Cell assembly.—A 10 Ah pouch cell, in the following referred to as "KIT_10," with integrated FBG sensors was assembled in a dry room (dew point −60 °C) by use of the semi-automated production line at the Battery Technology Center at Karlsruhe Institute of Technology as described in a previous study.[51] The cell includes a stack of nine double-sided coated cathodes (NMC111, purchased commercially), ten double-sided coated anodes (graphite, purchased commercially), as well as 20 layers of ceramic-coated PET separator placed in between alternating cathodes and anodes and as outer layers on bottom and top of the cell stack. The cathode, anode and separator sheets are 13.5 cm × 20.8 cm, 13.9 cm × 21.2 cm, and 14.3 cm × 21.6 cm in size, respectively. The glass fiber was placed on top of the cell stack, including two FBG sensors located approx. 1 cm below each current collector tab as indicated in Fig. 1b and in the photograph in Fig. 2. The fiber was fixed with adhesive tape at the far left and right end of the cell stack, to avoid any interference with the sensors. All components, excluding the fiber sensor, which was dried using a heat gun under dry room conditions, were dried under reduced pressure at 130 °C for 24 h. The cell was filled with 35.7 ml of electrolyte (1 M LiPF$_6$ in EC:DMC (1:1) + 3 wt% VC, purchased from Gotion), sealed under reduced pressure and stored overnight at 40 °C for homogeneous wetting. Secondly, a 20 Ah pouch cell, referred to as "KIT_20" in the following, was built with two same sized cell stacks as that of the KIT_10 cell with the fiber being placed in the center of the cell including nine FBG sensors

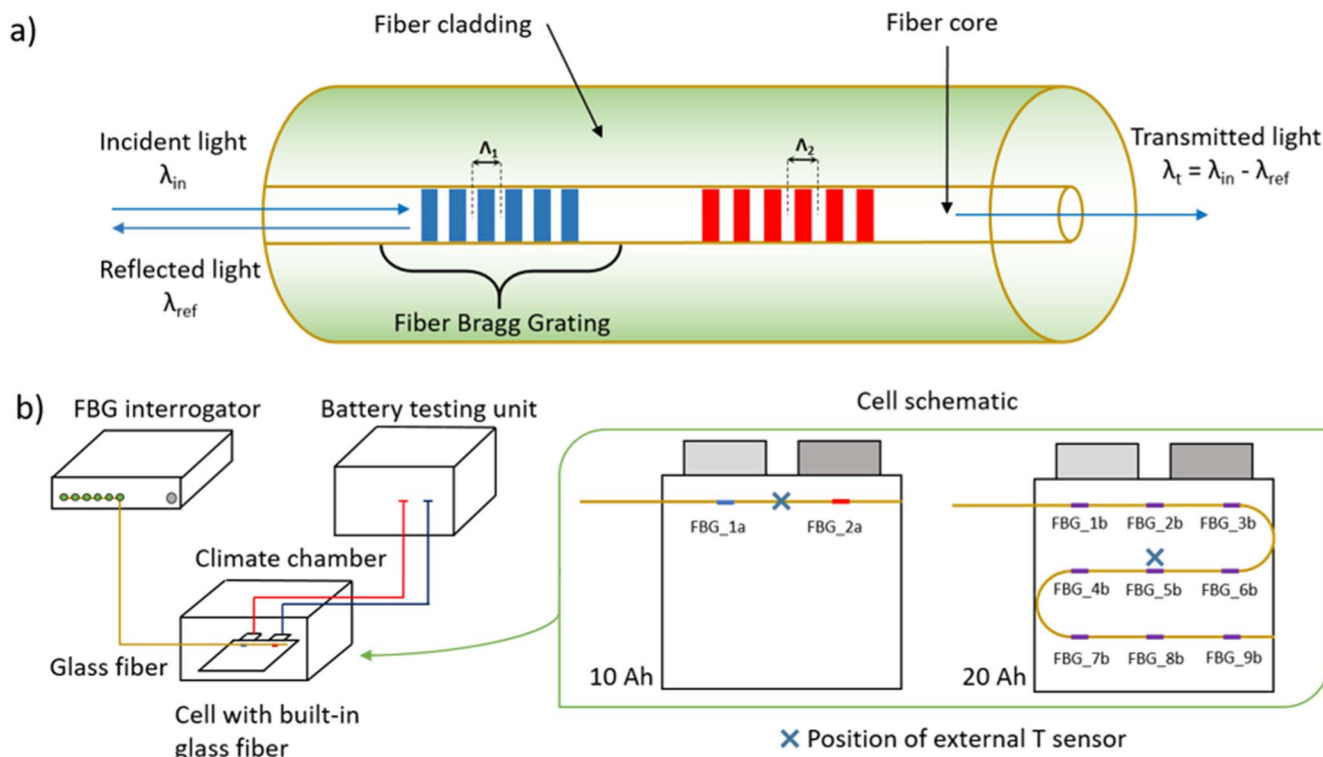**Figure 1.** Schematic of the working principle of the FBG-sensors with Λ_1 and Λ_2 representing two individual sensors within one fiber (a) and the experimental setup for in situ temperature measurements (b). Note that for the 10 Ah cell (KIT_10) the fiber is placed on top of the cell stack, whereas for the 20 Ah cell (KIT_20) the fiber is sandwiched in between two 10 Ah electrode stacks.

Table I. Nomenclature of variables used for the calibration model and further analysis in the order in which they appear in the text.

Name	Description	Unit
SoC	State of charge	%
λ_{in}	Wavelength of incoming beam	nm
λ_{ref}	Base wavelength of an FBG sensor	nm
λ_t	Wavelength of transmitted beam	nm
Λ	Spacing of sensor grating	nm
n_{eff}	Refractive index of fiber core	
U_{max}	Upper cut-off voltage	V
U_{min}	Lower cut-off voltage	V
U_N	Nominal voltage	V
λ_{raw}	Wavelength raw data signal	nm
$\Delta\lambda_{UN}$	SoC-affected wavelength shift at U_N (SoC ≠ 0%)	nm
$\Delta\lambda_{EQU}$	Wavelength shift due to relaxation in OCV step	nm
λ_{mean}	1 h average wavelength at constant SoC and constant temperature	nm
λ_T	Strain-free temperature-induced wavelength	nm
T	Temperature	°C
$\lambda_{0\,°C}$	Strain-free temperature-induced wavelength at 0 °C	nm
k	Linear regression coefficient of temperature calibration	nm/°C
m_{SoC}	Linear regression of SoC-dependent strain calibration	nm/%
$\Delta\lambda_{inc}$	Strain-induced wavelength change in SoC increment	nm
ΔSoC_{inc}	Change in SoC in one SoC increment	%
λ_0	Wavelength at 0% SoC	nm
$\Delta\lambda_\varepsilon$	Temperature-free strain-induced wavelength change	nm
$\lambda_{inc,0}$	Wavelength at the beginning of one SoC increment	nm
SoC_{inc}	SoC at the beginning of one SoC increment	%
ε_f	Mechanical strain	
n_0	Average refractive index of sensor grating	
ν_f	Poisson's ratio	
p_{11}, p_{12}	Strain-optic coefficients of optical fiber	
σ	Stress	Pa
E	Elastic modulus	Pa
$\Delta\lambda_{\varepsilon,irrev}$	Wavelength change induced by irreversible strain	nm
T_{max}	Maximum temperature	°C
$\Delta T_{max,\,internal-external}$	Difference in external and internal maximum temperature	°C
$\Delta t_{external-internal}$	Offset time between external and internal T_{max} detection	s

(FBG_1b to FBG_9b) evenly distributed in the plane as can be seen in Fig. 1b as well as in a photograph shown in the supporting information (SI) (Fig. S1). Here, the fiber was also fixed with adhesive tape at several positions to the separator with sufficient distance to each sensor. Electrode materials and separator were the same as those of the KIT_10 cell and 70 ml of the same electrolyte was used. The surface area of the cell stacks of both cells is 208.8 cm² and the cell thickness is 3.1 mm and 5.9 mm of the KIT_10 and the KIT_20 cell, respectively.

Setup for measurements.—Figure 1b depicts the principle experimental setup including the Li-ion pouch cell with an integrated
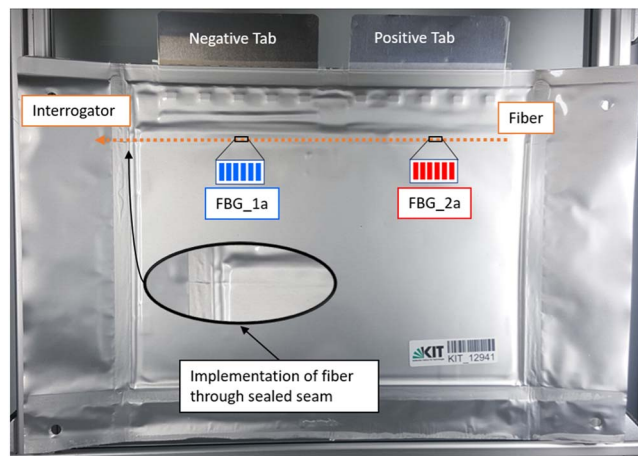

Figure 2. Photograph of the KIT_10 Li-ion pouch cell containing a glass fiber with two FBG sensors. The glass fiber is placed below the current collector (indicated by orange dotted line). FBG sensor positions are indicated by black rectangles with FBG_1a on the left and FBG_2a on the right. Inset: Zoom-in on the position where the glass fiber runs through the sealed seam of the cell.

optical fiber. The cell is located in a climate chamber and connected to a potentiostat. The fiber is connected to an interrogator that is at the same time source and detector of the incident and reflected light, respectively. External NTC5K temperature sensors were attached with thermally conductive adhesive pads on the pouch foil surface approx. in between the positions of FBG_1a and FBG_2a and above FBG_5b.

Instrumentation.—Cell formation was performed using a BasyTec MRS cycler. Further cell cycling was performed by use of a BasyTec X40 cycler. For external temperature measurements on top of the pouch cells a NTC5K sensor (purchased from TDK Group) was used. The NTC5K sensor was connected with the cycler and temperature data was logged by the Basytec software with a collection rate of 1 Hz. During all measurements a systematic offset of the NTC5K sensor of approx. +0.37 °C and +0.3 °C for KIT_10 and KIT_20 cell, respectively, was detected that was subtracted from the raw data. Temperature and strain calibration of the FBG sensors and subsequent cycling were performed in a Binder climate chamber (model KB115) with a nominal temperature window of −5 to 100 °C. Optical glass fibers with FBG sensors and an industrial BraggMETER FS22 interrogator were purchased from HBK Hottinger Brüel & Kjaer GmbH and used as received. Monitor rate was adjusted to 1 Hz to match the monitor rates of the Basytec devices.

For initial formation, the cells were charged with constant current constant voltage (CCCV) at C/10 until the upper cut-off voltage $U_{max} = 4.2$ V (CC) was reached and subsequently held at U_{max} until current I < C/20 (CV), followed by constant current (CC) discharge with C/2 to the lower cut-off voltage $U_{min} = 3.0$ V. Subsequently, the cell underwent two full CCCV-charge (CV until I < C/20) and CC-discharge cycles using a C-rate of C/2 in a voltage range from U_{min} to U_{max}. At the end of the formation the cell was CC-charged to the nominal voltage of $U_N = 3.7$ V with C/2. The cell was then opened, degassed and re-sealed.

In order to exclude a possible influence of the fiber on the electrochemical performance of the cells, the charge/discharge potentials during formation as a function of capacity were compared with those of an identical FBG-free reference cell presented by Smith et al.[51] (see Fig. S2). The capacity was normalized to the active cathode area (double-sided coated) in order to eliminate the effect of different number of layers in the stack of the KIT_20 cell. The data ensure proper electrochemical properties of the cells equipped with sensors.

Strain calibration for the KIT_10 cell was performed by CC-discharge to U_{min} at C/20, followed by a C/20 cycle (CC-charge and CC-discharge) to determine the exact cell capacity. Afterwards the cell was charged and discharged at C/20 in steps of 2.5% SoC according to the measured cell capacity. After each 2.5% SoC step a pause of 2 s was implemented as a timestamp for the subsequent data evaluation. Finally, the cell was charged to U_N again. For the KIT_20 cell the current was lowered to C/40 to avoid thermal influences by internal cell processes during charge and discharge.

After strain calibration, a rate test was performed using varying discharge rates of C/2, 1C, 2C, 3C, 4C and again C/2 for two cycles each. Charging was performed with a C-rate of C/2 (CCCV for 10 Ah cell (CV at U_{max} until I < C/20) and CC for the 20 Ah cell). The climate chamber was set to 25 °C for these operations.

The temperature calibration was carried out in the typical temperature range for battery operation of 20 °C to 38 °C with steps of 2 °C. Prior to the calibration the cell was charged to the nominal voltage U_N = 3.6 V and remained at OCV during the calibration. At each temperature step, the data recording was preceded by a waiting period of at least 8 h to ensure a stable temperature in the climate chamber and a uniform temperature distribution in the cell. FBG sensor data was then recorded for 1 h with a data collection rate of 1 Hz. Data for temperature calibration was collected after the strain calibration before the rate test for the KIT_10 cell and after the strain calibration and the rate test for the KIT_20 cell.

Results and Discussion

The temperature- and strain-induced changes in reflected wavelength were determined for all internal FBG sensors individually. Hereafter, the sensors will be referred to as FBG_1a and FBG_2a for the KIT_10 cell and FBG_1b to FBG_9b for the KIT_20 cell as indicated in Fig. 1b. In particular, FBG_5b will be shown throughout the discussion of the KIT_20 cell results as all sensors in this cell behave similar as shown in the SI (Figs. S3 to S5). The entire calibration of the sensors was carried out after they had already been installed inside the cells. To allow for a differentiation of the temperature- and strain-induced fraction of the measured wavelength raw data λ_{raw} and a calculation of actual temperature inside the cells, two separate calibration steps were performed. During temperature calibration the cell was kept at open circuit voltage (OCV) at a constant SoC, to avoid any temperature evolution and to keep the existing strain on the FBG sensors constant. It is known from literature that thermal swelling plays a significant role in the expansion of rechargeable Li-ion cells, especially at high C-rates.[52,53] By calibrating the fiber to the temperature in the already installed position in the cell, it was possible to take these effects into account so that precise temperature determination could be carried out in further measurements even at higher C-rates and correspondingly higher cell temperatures. Strain calibration on the other hand requires the cell to be charged/discharged to various SoC leading to different strain responses, however, it also requires a constant temperature. Given the fact that electrochemical processes within the cell will always give a thermal response, this effect needs to be minimalized. For the KIT_10 cell this was achieved by cycling at a very low C-rate of C/20, whereas the thicker KIT_20 cell had to be cycled at C/40. In addition to the FBG sensors, the cell surface temperature was constantly monitored by the external NTC5K temperature sensor. In the following, the temperature and strain calibration will be explained in detail.

Temperature calibration.—Prior to temperature calibration the cell was charged to U_N = 3.7 V with a rate of 1 C and rested at OCV during calibration. In response to this change in SoC, a change in the measured wavelength signal is detected and two major effects need to be considered for proper calibration. For a better understanding, a visualization of these effects is given in Fig. 3a. Firstly, as the cell was charged to U_N prior to data collection, strain is already applied to the sensors as the cell is no longer at 0% SoC. This SoC-affected
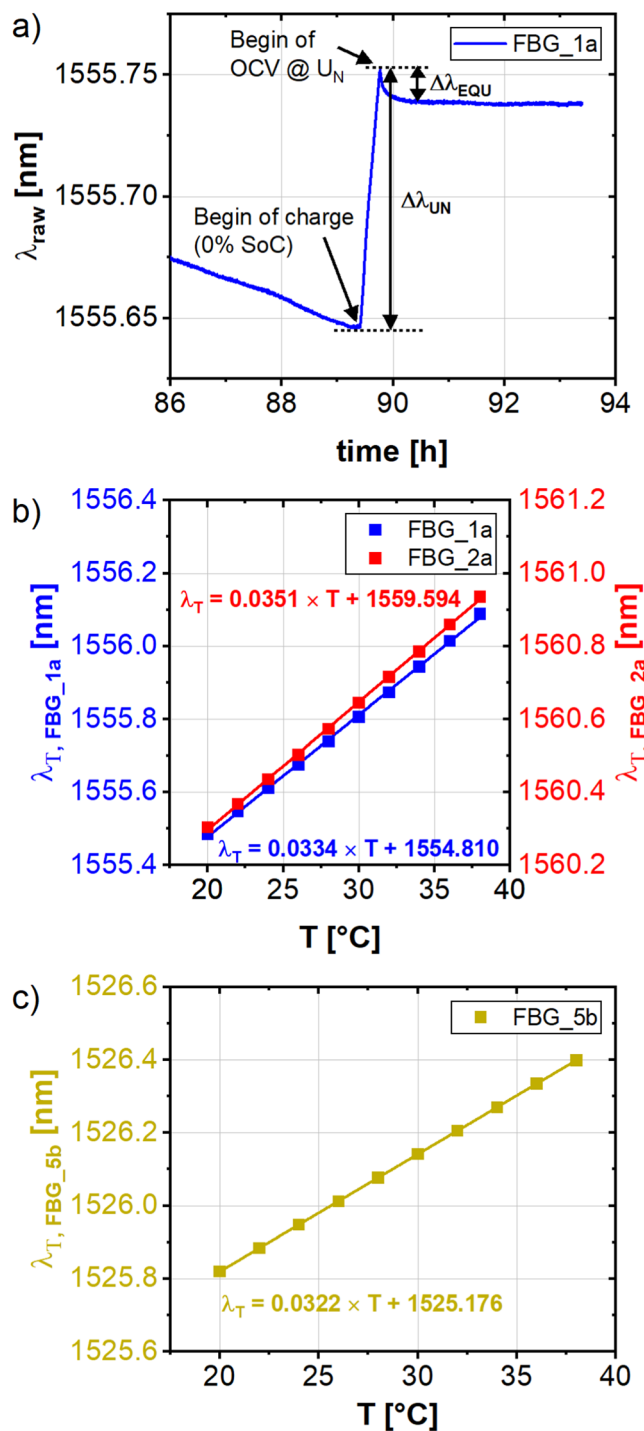

Figure 3. (a) Evolution of wavelength signal of FBG_1a during charging to U_N and relaxation of the wavelength during the OCV step prior to temperature calibration of sensor FBG_1a. Notably, the sensor data need approximately 30 min to reach equilibrium. The data shown was acquired after strain calibration and the rate performance test. (b) Temperature calibration curves for sensors FBG_1a and FBG_2a. (c) Temperature calibration curve for sensor FBG_5b.

wavelength shift $\Delta\lambda_{UN}$ has to be taken into account. Secondly, at the beginning of the OCV period, a relaxation of measured wavelength $\Delta\lambda_{EQU}$ is observed that equilibrates over time. This relaxation is assumed to be related to Li diffusion processes in the electrode materials and equilibration of Li concentration within the active material particles. Also, an observed increase in temperature during charging to U_N that declines during the rest step contributes to the

equilibration process. As the calibration is applied for evaluation of data taken during dynamic charging/discharging of the cells, relaxation effects were not considered and $\Delta\lambda_{EQU}$ must be deducted.

For temperature calibration the climate chamber was then set successively from 20 °C to 38 °C in steps of 2 °C and wavelength signals were monitored. After a stable temperature in the climate chamber and complete thermal equilibration of the cell was guaranteed (after a sufficiently long equilibration time of 8 h), FBG sensor data was recorded for 1 h and the mean value λ_{mean} is calculated. Then, by subtracting $\Delta\lambda_{UN}$ and $\Delta\lambda_{EQU}$ the actual strain-free wavelength λ_T, corresponding to conditions at 0% SoC at the respective set temperature, is determined according to Eq. 3.

$$\lambda_T = \lambda_{mean} - \Delta\lambda_{UN} - \Delta\lambda_{EQU} \qquad [3]$$

It should be noted that $\Delta\lambda_{EQU}$ has a negative or positive value, depending on whether the cell voltage was set to U_N by charging or discharging. Figure 3 shows the calibration data λ_T of the sensors FBG_1a and FBG_1b (Fig. 3b) and FBG_5b (Fig. 3c) together with linear calibration curves. From linear regression the temperature can then be calculated via Eq. 4

$$T = \frac{\lambda_T - \lambda_{0\circ C}}{k} \qquad [4]$$

with k and $\lambda_{0\,°C}$ representing the slope and the wavelength for 0 °C, respectively.

Strain calibration.—In the second part of the two-step calibration, the sensitivity of FBG sensors towards changes in strain, which are caused by volume expansion/contraction of the cell stack during cycling, is accounted for. A calibration of absolute pressure values is rather challenging, as applying various pressures for reference could have impact on the electrical and electrochemical properties of the cell. Instead, the SoC of the cell can be used as a simplified reference for wavelength changes resulting from changes in cell stack volume. The direct relation of SoC and cell expansion of an identical FBG-free reference cell (corresponding to the 10 Ah cell presented in here) was examined by Nazari et al.[54]

For strain calibration the cells underwent a full CCCV-charge and CC-discharge cycle for capacity determination followed by a second cycle in which the cells were charged and discharged in 2.5% SoC steps between 0% and 100% SoC. A short rest step of 2 s was applied between each 2.5% SoC step serving as an indicator for the following data analysis. Then, an incremental fit was applied to the wavelength data. In case of the 10 Ah cell the curve was divided in increments according to the 2.5% SoC steps of the second calibration cycle. In case of the 20 Ah cell the input data was further subdivided in increments of 1% SoC in order to demonstrate the improving effect on the resolution of the mathematical procedure and the following results (see discussion below). For each SoC increment for charge and discharge direction the regression coefficient m_{SoC} for the strain-induced linear slope was determined according to (Eq. 5)

$$m_{SoC} = \frac{\Delta\lambda_{inc}}{\Delta SoC_{inc}} \qquad [5]$$

with $\Delta\lambda_{inc}$ being the change in wavelength for an increment and ΔSoC_{inc} being the change in SoC within an increment. This yields 80 regression coefficients for the KIT_10 cell (Table S1) and 200 regression coefficients for the KIT_20 cell (Tables S2 and S3) which are available in look-up tables for further data processing. Based on the prerequisite that no temperature evolution occurs at the slow C-rates, these slopes purely describe the strain-induced wavelength change of the sensors and, therefore, (Eq. 6) is valid:

$$\lambda_{raw} - \lambda_0 = \Delta\lambda_\varepsilon \qquad [6]$$

with λ_0 being the wavelength at 0% SoC and $\Delta\lambda_\varepsilon$ being the strain-induced proportion of measured wavelength.

Therefore, for further data acquired at higher C-rates, a subtraction of $\Delta\lambda_\varepsilon$ will result in the strain-free wavelength signal that can purely be related to temperature changes.

Eventually, the change in measured wavelength induced by reversible strain over the complete SoC range can be described by the following equation (Eq. 7)

$$\Delta\lambda_\varepsilon = (\lambda_{inc,0} - \lambda_0) + m_{SoC} * (SoC - SoC_{inc}) \qquad [7]$$

with $(\lambda_{inc,0}-\lambda_0)$ being the difference between the wavelength at 0% SoC and the wavelength at the beginning of the increment and $(SoC-SoC_{inc})$ the difference between the SoC and the SoC at the beginning of the according increment.

By subtracting $\Delta\lambda_\varepsilon$ from the raw data signal the resulting wavelength can purely be related to temperature changes (Eq. 8).

$$\lambda_T = \lambda_{raw} - \Delta\lambda_\varepsilon \qquad [8]$$

Moreover, from the strain-induced shift in wavelength $\Delta\lambda_\varepsilon$ the mechanical strain ε_f can be calculated by solving the following equation:[55]

$$\frac{\Delta\lambda_\varepsilon}{\lambda_0} = \left(1 - \frac{n_0^2}{2}[p_{12} - \nu_f(p_{11} + p_{12})]\right)\varepsilon_f \qquad [9]$$

where n_0 is the average refractive index of the grating, ν_f is the Poisson's ratio and p_{11} and p_{12} are strain-optic coefficients of the optical fiber. The strain can then be converted to a stress σ using Hooke's law:

$$\sigma = E\varepsilon_f \qquad [10]$$

with the elastic modulus E.

Additional considerations and correcting terms.—Besides reversible volumetric changes in the electrodes, irreversible processes (e.g. SEI formation, gas formation due to electrolyte and active material decomposition and associated internal pressure increase) might possibly impact the measured strain-induced wavelength signal. Therefore, any irreversible strain $\Delta\lambda_{\varepsilon,irrev}$, if observed, has to be taken into account. This yields to the following equation (Eq. 11) for the strain-free temperature-induced component λ_T of the measured wavelength:

$$\lambda_T = \lambda_{raw} - \Delta\lambda_\varepsilon - \Delta\lambda_{\varepsilon,irrev} \qquad [11]$$

Finally, it should be noted that the method presented is a simplified approach in which the T-induced and strain-induced components of the fiber signal are determined under conditions that correspond more closely to a relaxed state. At higher C-rates additional stress components contribute to the measured signal due to heterogeneity of the phase fractions and Li concentration in the electrodes.[56] These components cannot be differentiated with this method due to the restriction on the $\Delta\lambda_\varepsilon$ variations based on the respective SoC values. Various studies[57–59] have analyzed the effects of non-uniform intercalation/de-intercalation on the strain signal. However, heat generation at high C-rates also favors the kinetic processes, as investigations of the relaxation time have shown,[56] which simultaneously counteracts this SOC-heterogeneity.

Implementation of calibration method.—By way of example, the calibration approach is presented for the KIT_10 cell (see Figs. S3 and S4 for calibration data of KIT_20 cell). Figure 4a shows the electrochemical data (current I, cell voltage U) during the two cycles of strain calibration of the KIT_10 cell. Figure 4b shows the measured wavelength signal λ_{raw} of the two integrated sensors
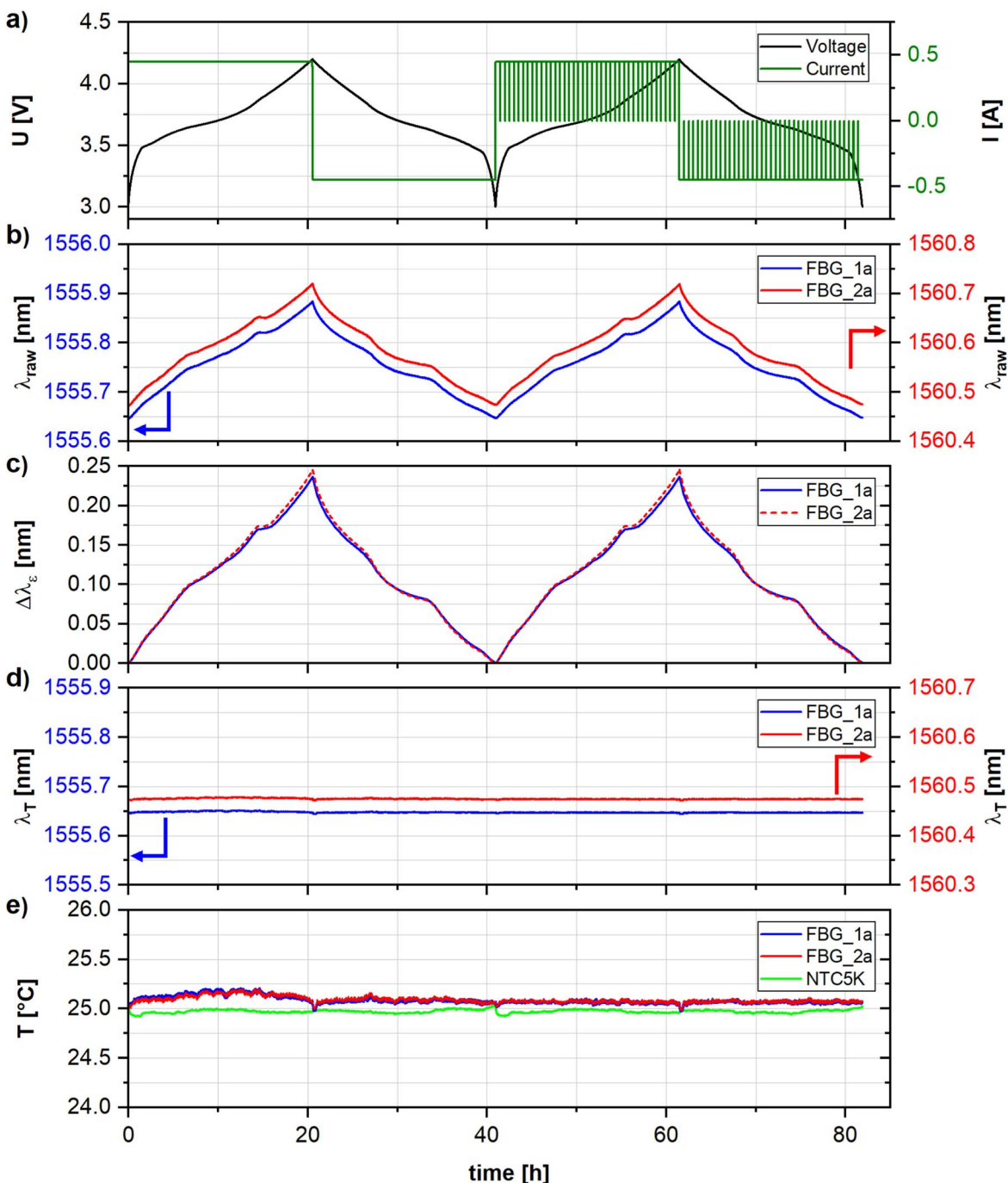
Figure 4. Results of strain calibration measurements of KIT_10 cell containing (a) voltage and current, (b) FBG_1a and FBG_2a sensor raw data, (c) calculated strain-induced proportion of measured wavelength change (d) calculated temperature related wavelength signal and (e) calculated cell temperature based on FBG data in comparison to data from the external NTC5K temperature sensor.

FBG_1a and FBG_2a. The wavelength increases and decreases reversibly upon charge and discharge, reflecting the expansion and contraction of the cell stack.

It has to be noted that the observed wavelength change can also be due to irreversible volume changes, which is however unlikely as the wavelength signal declines back to almost the same value at 0% SoC at the end of each cycle. Figure 4c shows the reversible strain-induced wavelength change of both sensors calculated by use of Eq. 7, which basically equals the change in measured raw data. As can be seen in Figs. 4d and 4e, the calculated temperature-induced fraction of wavelength λ_T and resulting calculated temperature is nearly stable according to the fundamental assumption that all

wavelength change can be assigned to strain effects. Also, the temperature measured by the external NTC5K sensor is nearly stable over the course of strain calibration confirming the assumption that a slow charge and discharge rate of C/20 is sufficiently low to guarantee a constant cell temperature for the KIT_10 cell.

However, as the mathematical description of the strain-induced wavelength course is solely a simplified approximation, minor fluctuations can still be detected in the calculated temperature signal and these artefacts are affected by the restricted resolution of fitting increments of 2.5% SoC. This can be improved by the higher resolution of 1% SoC used for the KIT_20 cell as shown in the SI in Fig. S3.

Application on rate performance test.—To evaluate the performance of the proposed calibration method it was applied on FBG data acquired during a rate capability test. Figure 5 shows the electrochemical data (Fig. 5a) together with the FBG data (Figs. 5b –5d) and calculated and measured temperature data (Fig. 5e) of the KIT_10 cell. During the first two cycles with moderate charge and discharge rate of C/2, coherent wavelength signals λ_{raw} (Fig. 5b) are detected by the two FBG sensors FBG_1a and FBG_2a with reproducible values at the end of charge (EoC) and the end of discharge (EoD). As the discharge rate increases, changes in the course of λ_{raw} are detected, notably the wavelength does no longer reach the initial values but successively reaches higher values at EoD. By following the calibration procedure, the strain-induced fraction of

measured wavelength $\Delta\lambda_\varepsilon$ can be considered separately (Fig. 5c). As it can be seen, the increasing wavelength at EoD can in some extent be traced back to irreversible change in $\Delta\lambda_\varepsilon$ which is attributed to a decreasing depth of discharge (DoD) with higher C-rates. An increasing polarization at higher amperage prevents the cell from full discharge to 0% SoC and strain associated with a volume increase of the cell stack, that is built up during charge, is not fully reversed in the following discharge cycle. It should also be noted that even though the two sensors FBG_1a and FBG_2a have different base wavelengths, they both show the same wavelength shift upon charging and discharging also at higher C-rates, indicating that strain changes take place homogeneously in the plane of the cell stack (at least with regard to the two different positions of the sensors). This is also
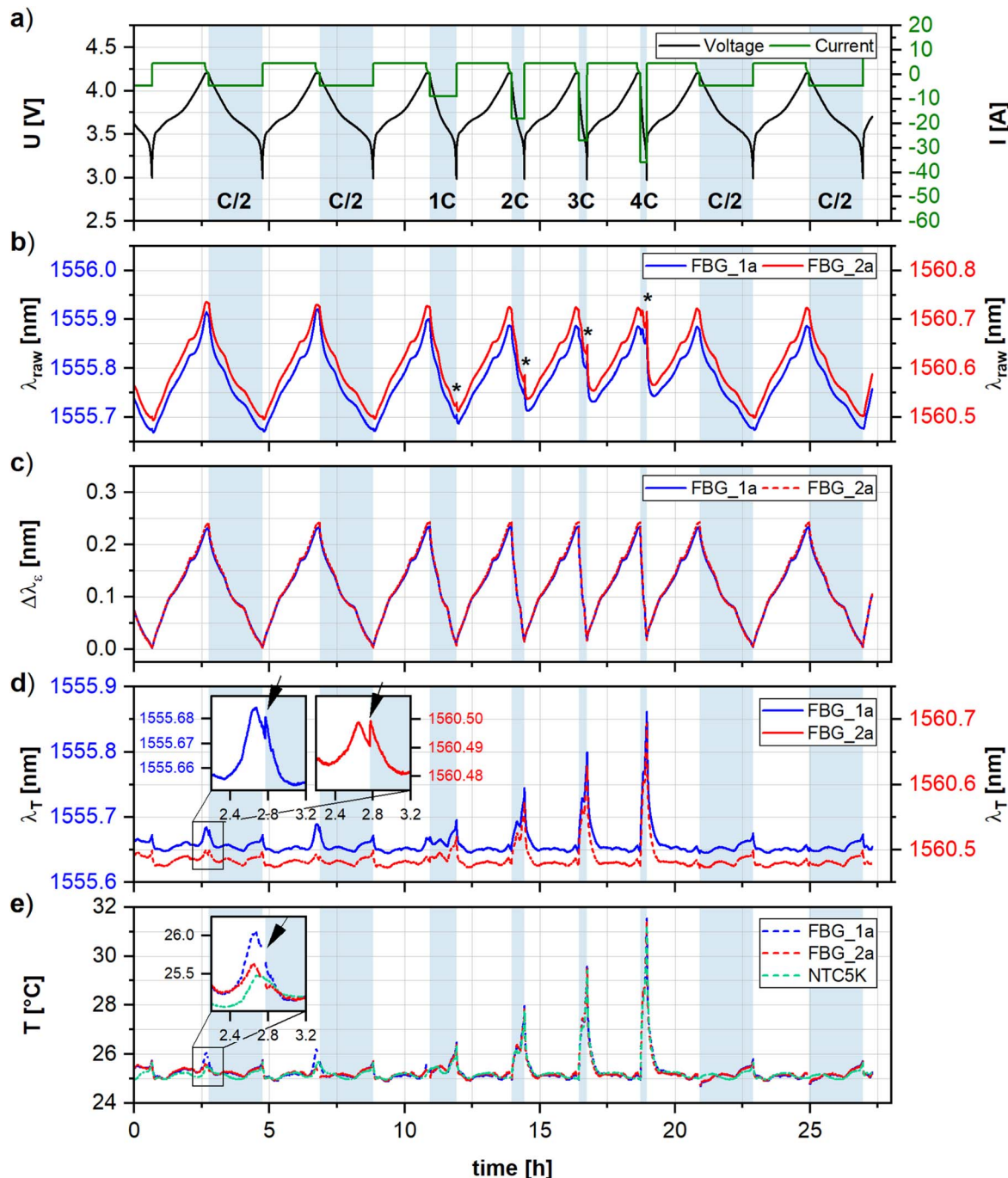

Figure 5. Results from rate capability test of the KIT_10 cell containing (a) voltage and current, (b) FBG_1a and FBG_2a sensor raw data, (c) calculated strain-induced proportion of measured wavelength change (d) calculated temperature related wavelength signal and (e) calculated cell temperature based on FBG data in comparison to data from the external NTC5K temperature sensor.

indicated by the results of the KIT_20 cell (see data of all nine sensors in Fig. S5 of the SI). An additional peak is observed in λ_{raw} during each discharge cycle with discharge rate >C/2, showing increasing peak height with increasing C-rate (marked by asterisks in Fig. 5b). By subtracting $\Delta\lambda_\varepsilon$ from λ_{raw} the strain-free wavelength signal λ_T, that is purely related to temperature changes is obtained (Fig. 5d) and by further applying the temperature calibration the absolute cell temperature is achieved (Fig. 5e).

The data show that the additional peaks in λ_{raw} are attributed to heating of the cell during discharge with increasing C-rate. The detected temperature increase reaches maximum values at the end of each discharge cycle. This also strongly contributes to the observed increasing wavelength signal λ_{raw} at EOD with increasing C-rate. Overall, the temperature inside the cell measured by the FBG sensors is in good accordance with the cell surface temperature measured by the NTC5K sensor (also shown in Fig. 5e and summarized in Table II with discussion below).

The results of the FBG_5b sensor of the 20 Ah cell is shown in Fig. 6 (see results of the other eight sensors of the KIT_20 cell in Figs. S5 and S6). It has to be noted that some minor irreversible changes in the wavelength signal were observed over the period of the performed experiments. These are assumed to be related to aging effects and pressure increase due to gas formation which contribute by $\Delta\lambda_{\varepsilon,irrev}$ to the calculation according to Eq. 11. Therefore, a correcting procedure was applied to the raw data resulting in the corrected wavelength signal as shown in Fig. 6b (detailed description in SI). The wavelength data appear very similar to that of the KIT_10 cell with comparable peaks due to heating at higher C-rates (also marked by asterisks in Fig. 6b) and decreasing drops in measured wavelength at EOD caused by heating and due to decreasing DoD. The calculated values for the cell temperature are, again, in good accordance with the ones of the external NTC5K sensor (Fig. 6e). It should be mentioned that some artefacts are observed in the data of both cells. For FBG_1a and FBG_2a, a relaxation of λ_{raw} is detected at EOC during the CV step that is traced back to strain relaxation in the electrodes probably due to lithium diffusion and equilibration of lithium concentration. This is, however, not considered by the SoC-based strain calibration that assumes only constant current, i.e. constant change in SoC, which is not given during CV charge.

This limitation of the calibration method leads to artefacts in the calculated λ_T and data gaps in the calculated temperature (marked exemplarily for FBG_1a and FBG_2a for the first charge cycle by arrows in the inlets in Figs. 5d and 5e). In case of the KIT_20 cell this effect can be eliminated due to the absence of the CV steps. Nonetheless, there are still some additional very small artefacts in λ_T at the EOC for both cells appearing as discontinuous jumps (also visible in the inlet in Fig. 5d and marked exemplarily for FBG_5b by an arrow in the inlet in Fig. 6d). These occur during the transition from charge to discharge in case that 100% SoC is not entirely reached at EOC. Then, the strain calibration is subjected to a discontinuous misfit of linear regression coefficients due to strain hysteresis (see Fig. 8a and discussion below).

Figure 7 depicts a more detailed view of temperature data of both cells at cycles with higher discharge rates. Please note that the temperature increase and the data gaps of FBG_1a and FBG_2a marked by triangles in Fig. 7a result from artefacts as discussed above. Besides a rather linear increase in temperature over the course of discharge a remarkable change in slope marked as region I can be observed in each cycle. At the end of each discharge cycle the temperature reaches a maximum marked as region II. The underlying cause of change in temperature evolution in region I is unclear but it was also observed by others, for example by Li et al. inside 25 Ah pouch cells by use of thermocouples[60] and by Li et al. performing surface temperature and strain measurements on commercial 30 Ah pouch cells by use of FBG sensors.[61] The change in slope might be associated with kinetic effects due to phase transformations in the electrodes, most likely in the graphite anode as there are also indications for kinetic limitations in the data of $\Delta\lambda_\varepsilon$ as shown in Fig. 8a. The data refers to the calibration cycle of the KIT_10 cell with charge and discharge rates of C/20 where temperature effects are assumed to be neglectable. There is a significant hysteresis in $\Delta\lambda_\varepsilon$ between charge and discharge.

Also, the signal of $\Delta\lambda_\varepsilon$ shows significant changes in slope at approx. 35% and 70% SoC during charge but less pronounced features during discharge.

Identical behavior is observed for the KIT_20 cell (see Fig. S7 for corresponding data of FBG_5b) and clear similarities could also be observed for a KIT_20 cell via real-time thickness measurements.[54] This observation is emphasized in Fig. 8b where the strain-induced linear slope m_{SoC} is shown as function of SoC. It may point to polarization effects during discharge leading to enhanced heating in region I followed by a decrease in heating rate as the polarization is overcome. Possible reasons for the observed hysteresis may be staging-effects in graphite as discussed in literature.[62]

The measurements show that the change in heating rate in region I is also detected by the external NTC5K sensors for both cells (Fig. 7), however, with less detailed resolution compared to the internal sensors. For all C-rates after the turning point in temperature region I is reached the temperature flattens off and then further increases until the end of discharge where the maximum temperature of each cycle, marked as temperature region II, is reached. To compare the sensitivity of internal FBG and external NTC5K sensors and the influence of sensor position on detected temperature, a summary of maximum temperature T_{max}, difference in external and internal maximum temperature $\Delta T_{max,\ internal-external}$ and offset time between external and internal sensors $\Delta t_{external-internal}$ is given in Table II. A comparison of the FBG data of the two cells shows that significantly higher temperatures are present in the center of the KIT_20 cell (FBG_5b) compared to the top of the cell stack of the KIT_10 cell (FBG_1a and FBG_2a). This is quite reasonable as, on

Table II. Comparison of maximum temperature measured by internal FBG and external NTC5K sensors during discharge at different C-rates as well as resulting temperature difference and offset time between internal and external sensors.

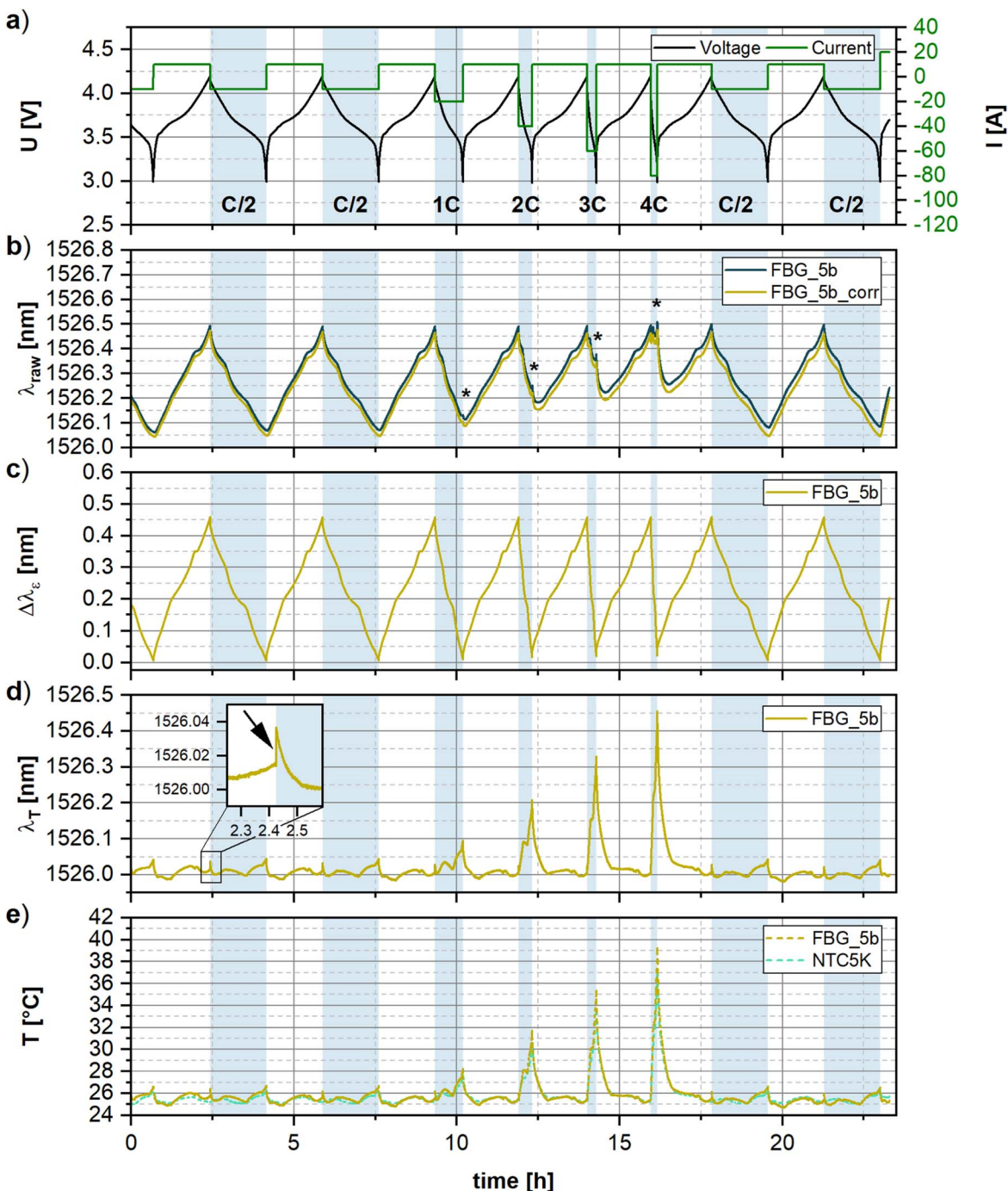| C-rate	T_{max} [°C]			$\Delta T_{max,\ external-internal}$ [°C]		$\Delta t_{external-internal}$ [s]	
			KIT_10 cell				
	FBG_1a	FBG_2a	NTC5K	FBG_1a	FBG_2a	FBG_1a	FBG_2a
2C	27.97	27.82	27.79	0.2	0.0	7.2	7.2
3C	29.65	29.50	29.42	0.2	0.1	5.2	5.2
4C	31.54	31.37	31.28	0.3	0.1	5.2	5.2
			KIT_20 cell				
	FBG_5b	NTC5K		FBG_5b		FBG_5b	
2C	31.77	30.65		1.1		6.2	
3C	34.65	33.85		0.8		7.0	
4C	39.44	37.26		2.2		12.2	

Figure 6. Results from rate capability test of the KIT_20 cell containing (a) voltage and current, (b) FBG_5a sensor raw data and FBG_5a_corr after correction of irreversible changes, (c) calculated strain-induced proportion of measured wavelength change (d) calculated temperature related wavelength signal and (e) calculated cell temperature based on FBG data in comparison to data from the external NTC5K temperature sensor.

the one hand, regarding the sensor positions center vs top of cell stack, heat dissipation to the outside takes longer, especially across the electrode layers, and on the other hand, regarding the thickness of cell stacks, the KIT_20 cell stack with twice the number of electrode sheets also leads to higher heat generation. Also, different temperature variations of internal and external sensors of the two cells are observed. Regarding the sensor position on top of the cell stack, there is only minimal difference of approx. 0.2 °C between the internal and external temperature measured and no detectable C-rate dependence.

For the internal sensor FBG_5b located in the center of the KIT_20 cell, in turn, a temperature difference of approx. 1 °C at 2C

and 3C and more than 2°C at 4C discharge rate is observed. In comparison, FBG data of a commercial 18650 cell (NCA/graphite) by Fleming et al. indicate a significant temperature difference between the core and can of up to 6 °C during discharge and 3 °C during charge.[30] Surprisingly, Nascimento et al. also observed higher temperature differences of up to 3.3 ± 0.1 °C comparing internal FBG sensor data with external sensor data of single-layer LiFePO$_4$/graphite pouch cells in the end of the CV charge step after slow charge at C/3.[32] Also, there are significant differences in the delay of the external temperature detection regarding the point of maximum temperature. Interestingly, regardless of the C-rate, there is already some delay of approx. 5 to 7 s between the internal and
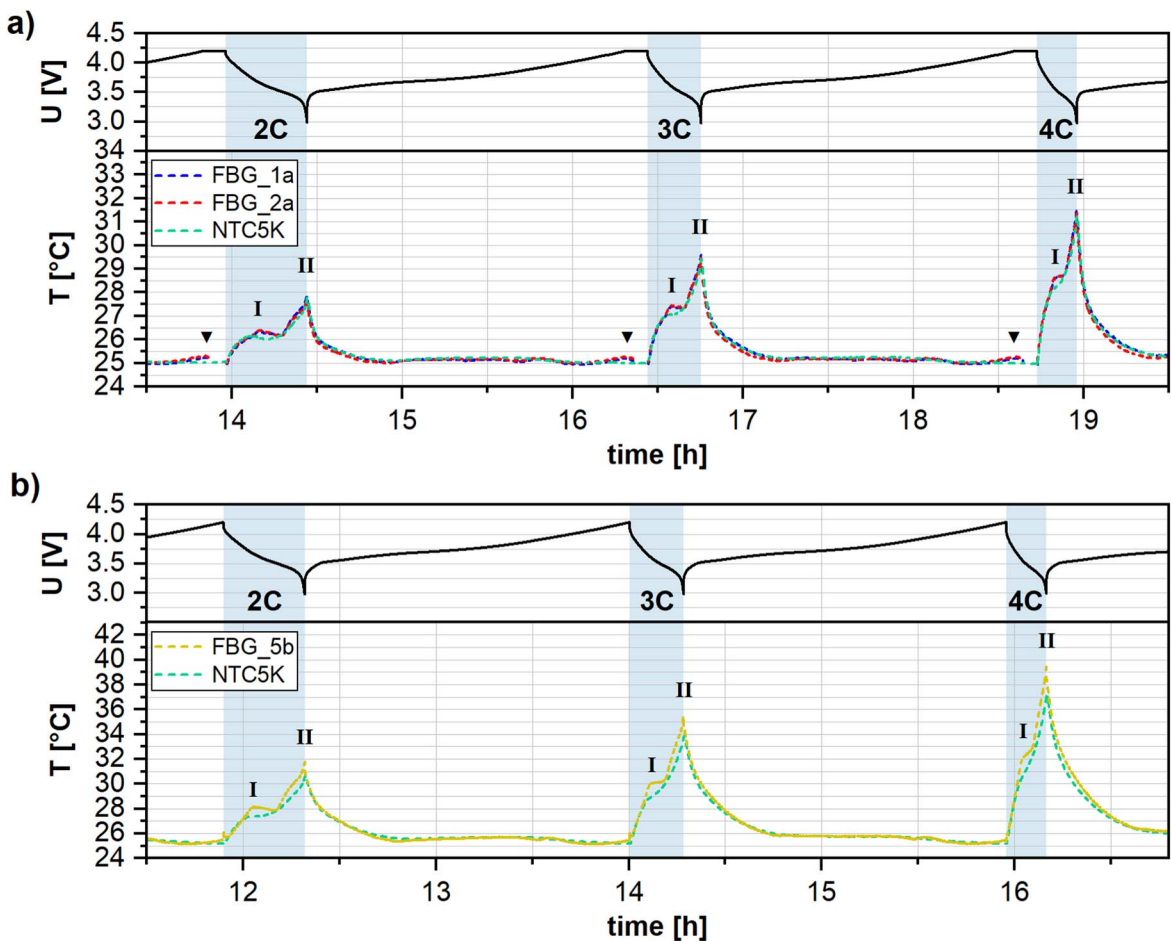
Figure 7. Calculated temperature together with temperature measured by the NTC5K sensors for increased discharge rates of (a) KIT_10 cell and (b) KIT_20 cell. The marked temperature regions I and II are discussed in text. Artefacts in the data of FBG_1a and FBG_2a resulting from non-linear change in SoC are marked by triangles and need to be neglected.

external sensors of the KIT_10 cell although they are only separated by a sheet of pouch foil. In case of the KIT_20 cell the delay between the sensor in the center of the cell stack and the external sensor is, as expected, higher with approx. 6 and 7 s at 2C and 3C and more than 12 s at a discharge rate of 4C. This demonstrates the added value of internal cell sensing technique and its potential use for early detection and risk minimization in cells and battery systems.

There are also differences observed between the two cells and sensor configurations regarding the SoC-induced impact of applied stress. For the KIT_10 cell a maximum deviation of $\Delta\lambda_\varepsilon$ of approx. 0.24 nm and 0.25 nm can be detected for FBG_1a and FBG_1b, respectively, during charging at C/20 from 0 and 100% SoC which is in a similar range as FBG data measured on 15 Ah LG pouch cells by Sommer et al.[44] and Ganguli et al.[45] By use of Eqs. 9 and 10 and the coefficients given in Table III the strain and the stress are estimated to be $\varepsilon_f = 0.15$ and $\sigma = 13.3$ MPa for FBG_1a and $\varepsilon_f = 0.16$ and $\sigma = 13.7$ MPa for FBG_2a. In comparison, a maximum change $\Delta\lambda_\varepsilon$ of approx. 0.48 nm is detected by FBG_5b for the KIT_20 cell (Fig. S5) yielding a strain of $\varepsilon_f = 0.39$ and a stress of $\sigma = 27.3$ MPa. Thus, the stress built up inside the cell stack of the KIT_20 cell is higher by the factor of 2. This matches quite well with the numbers of active electrode layers in the cell stack that is exactly twice the number of those in the KIT_10 cell.

Using FBG sensors Li et al. detected a similar increase in ε of approx. 0.38 upon charging of a 30 Ah pouch cell with a thickness comparable to that of the KIT_20 cell.[61] If the determined stress is related to the area of the electrode stack, a pressure of 68 PSI and

141 PSI can be calculated for the KIT_10 cell and the KIT_20 cell, respectively. These results are in very good accordance with those of Louli et al. yielding a reversible pressure evolution of approx. 60 PSI caused by the reversible net volume expansion of electrodes of multilayer NCM/Gr pouch cells.[64]

Conclusions

In this work a new calibration method for FBG sensors for decoupled in situ measurements of internal temperature and strain in Li-ion pouch cells was applied. The presented calibration and measurement procedures eliminate the necessity of additional reference sensors as commonly used in previous studies. The measurements show that the SoC-dependent volume changes in the electrodes pose significant stress leading to a non-neglectable strain impact on the FBG signal. Particularly, in case of application of FBG sensors in large-format cells with thicker electrode stacks this needs to be taken this into account for a correct acquisition of temperature data.

The principal findings of the study are as follows: at an elevated discharge rate of 4C, there was only a slight discrepancy of approximately 0.2 °C between internal FBG and external sensor when the temperature was gauged inside the 10 Ah cell, but solely at the top of the electrode stack. However, a temperature difference of over 2 °C was identified between the center and cell housing of the 20 Ah cell, and a delay in the detection of temperature peaks by the external sensor of 12 s. It was also shown that strain data correlate with numbers of electrode layers in the stack and yield a stress of up to 27.3 MPa in the center of the 20 Ah cell.

Figure 8. (a) Wavelength change induced by reversible strain and (b) linear regression coefficients as functions of SoC. Both determined by incremental linear regression of measured wavelength during strain calibration of KIT_10 cell.

Table III. Parameters used for the calculation of the strain ε_f from the wavelength shift $\Delta\lambda$. The refractive index n_0 was taken from.[63] The values for Poisson's ration ν_f, and elastic modulus E as well as strain-optic coefficients p11 and p12 were taken from.[48]

n_0	ν_f	p_{11}	p_{12}	E [GPa]
1.47	0.19	0.113	0.252	69.9

These results emphasize the advantages of internal cell sensing technique and its potential use for early detection and risk minimization in cells and battery systems.

Acknowledgments

ORCID

Lea Leuthner https://orcid.org/0000-0001-8546-0388
Anna Smith https://orcid.org/0000-0002-3329-248X

References

1. A. Manthiram, "A reflection on lithium-ion battery cathode chemistry." *Nat. Commun.*, **11**, 1 (2020).
2. G. E. Blomgren, "The development and future of lithium ion batteries." *J. Electrochem. Soc.*, **164**, A5019 (2017).
3. T. Kim, W. Song, D. Y. Son, L. K. Ono, and Y. Qi, "Lithium-ion batteries: outlook on present, future, and hybridized technologies." *J. Mater. Chem. A*, **7**, 2942 (2019).
4. N. Nitta, F. Wu, J. T. Lee, and G. Yushin, "Li-ion battery materials: present and future." *Mater. Today*, **18**, 252 (2015).
5. M. Li, J. Lu, Z. Chen, and K. Amine, "30 years of lithium-ion batteries." *Adv. Mater.*, **30**, 1 (2018).
6. R. Stockhausen, L. Gehrlein, M. Müller, T. Bergfeldt, A. Hofmann, F. J. Müller, J. Maibach, H. Ehrenberg, and A. Smith, "Investigating the dominant decomposition mechanisms in lithium-ion battery cells responsible for capacity loss in different stages of electrochemical aging." *J. Power Sources*, **543**, 231842 (2022).
7. X. Han, L. Lu, Y. Zheng, X. Feng, Z. Li, J. Li, and M. Ouyang, "A review on the key issues of the lithium ion battery degradation among the whole life cycle." *ETransportation*, **1**, 100005 (2019).
8. J. Vetter, P. Novák, M. R. Wagner, C. Veit, K. C. Möller, J. O. Besenhard, M. Winter, M. Wohlfahrt-Mehrens, C. Vogler, and A. Hammouche, "Ageing mechanisms in lithium-ion batteries." *J. Power Sources*, **147**, 269 (2005).
9. A. Schmidt, A. Smith, and H. Ehrenberg, "Power capability and cyclic aging of commercial, high power lithium ion battery cells with respect to different cell designs." *J. Power Sources*, **425**, 27 (2019).
10. S. Bak, E. Hu, Y. Zhou, X. Yu, S. D. Senanayake, S. Cho, K. Kim, K. Y. Chung, X. Yang, and K. Nam, "Structural changes and thermal stability of charged LiNi." *Applied Materials and Interfaces*, **6**, 22594 (2014).
11. P. Lyu, X. Liu, J. Qu, J. Zhao, Y. Huo, Z. Qu, and Z. Rao, "Recent advances of thermal safety of lithium ion battery for energy storage." *Energy Storage Materials*, **31**, 195-220 (2020).
12. Z. Li, J. Huang, B. Yann Liaw, V. Metzler, and J. Zhang, "A review of lithium deposition in lithium-ion and lithium metal secondary batteries." *J. Power Sources*, **254**, 168 (2014).
13. M. Weiss et al., "Fast charging of lithium-ion batteries: a review of materials aspects." *Adv. Energy Mater.*, **11**, 2101126 (2021).
14. D. C. Lee, J. J. Lee, J. S. Kim, S. Cho, and C. W. Kim, "Thermal behaviors analysis of 55 Ah large-format lithium-ion pouch cells with different cell aspect ratios, tab locations, and C-rates." *Appl. Therm. Eng.*, **175**, 115422 (2020).
15. A. Tomaszewska et al., "Lithium-ion battery fast charging: a review." *ETransportation*, **1**, 100011 (2019).
16. S. Goutam, A. Nikolian, J. Jaguemont, J. Smekens, N. Omar, P. Van Dan Bossche, and J. Van Mierlo, "Three-dimensional electro-thermal model of li-ion pouch cell: Analysis and comparison of cell design factors and model assumptions." *Appl. Therm. Eng.*, **126**, 796 (2017).
17. M. Xu, Z. Zhang, X. Wang, L. Jia, and L. Yang, "A pseudo three-dimensional electrochemical-thermal model of a prismatic LiFePO$_4$ battery during discharge process." *Energy*, **80**, 303 (2015).
18. W. Song, M. Chen, F. Bai, S. Lin, Y. Chen, and Z. Feng, "Non-uniform effect on the thermal/aging performance of Lithium-ion pouch battery." *Appl. Therm. Eng.*, **128**, 1165 (2018).
19. D. Kong, G. Wang, P. Ping, and J. Wen, "Numerical investigation of thermal runaway behavior of lithium-ion batteries with different battery materials and heating conditions." *Appl. Therm. Eng.*, **189**, 116661 (2021).
20. L. Lu, X. Han, J. Li, J. Hua, and M. Ouyang, "A review on the key issues for lithium-ion battery management in electric vehicles." *J. Power Sources*, **226**, 272 (2013).
21. S. Yang, C. Ling, Y. Fan, Y. Yang, X. Tan, and H. Dong, "A review of lithium-ion battery thermal management system strategies and the evaluate criteria." *Int. J. Electrochem. Sci.*, **14**, 6077 (2019).
22. J. Huang, S. T. Boles, and J-M. Tarascon, "Sensing as the key to battery lifetime and sustainability." *Nat Sustain*, **5**, 194 (2022).
23. M. Duff and J. Towey, "Two Ways to Measure Temperature Using Thermocouples Feature Simplicity, Accuracy, and Flexibility." *Analog Dialogue*, **44**, 6 (2010), https://www.analog.com/en/resources/analog-dialogue/articles/measuring-temp-using-thermocouples.html.
24. A. Jinasena, L. Spitthoff, M. S. Wahl, J. J. Lamb, P. R. Shearing, A. H. Strømman, and O. S. Burheim, "Online internal temperature sensors in lithium-ion batteries: state-of-the-art and future trends." *Front. Chem. Eng.*, **4**, 804704 (2022).
25. W. Wang, Y. Zhang, B. Xie, L. Huang, S. Dong, G. Xu, and G. Cui, "Deciphering advanced sensors for life and safety monitoring of lithium batteries." *Adv. Energy Mater.*, **14**, 2304173 (2024).
26. G. Han, J. Yan, Z. Guo, D. Greenwood, J. Marco, and Y. Yu, "A review on various optical fibre sensing methods for batteries." *Renew. Sustain. Energy Rev.*, **150**, 111514 (2021).
27. Y-D. Su, Y. Preger, H. Burroughs, C. Sun, and P. Ohodnicki, "Fiber optic sensing technologies for battery management systems and energy storage applications." *Sensors*, **21**, 1397 (2021).
28. R. Wang et al., "Operando monitoring of ion activities in aqueous batteries with plasmonic fiber-optic sensors." *Nat. Commun.*, **13**, 1 (2022).
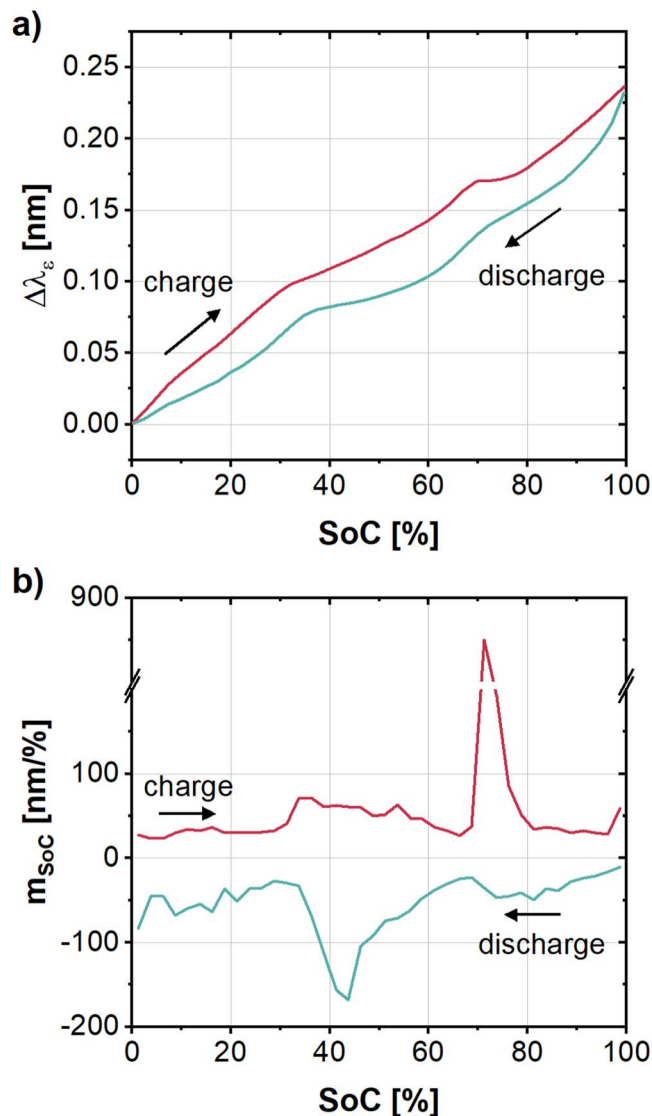
29. N. A. David, P. M. Wild, J. Hu, and N. Djilali, "In-fibre Bragg grating sensors for distributed temperature measurement in a polymer electrolyte membrane fuel cell." *J. Power Sources*, **192**, 376 (2009).

30. J. Fleming, T. Amietszajew, E. McTurk, D. Greenwood, and R. Bhagat, "Development and evaluation of in situ instrumentation for cylindrical Li-ion cells using fibre optic sensors." *HardwareX*, **3**, 100 (2018).

31. A. Fortier, M. Tsao, N. D. Williard, Y. Xing, and M. G. Pecht, "Preliminary study on integration of fiber optic bragg grating sensors in li-ion batteries and in situ strain and temperature monitoring of battery cells." *Energies*, **10**, 838 (2017).

32. M. Nascimento, S. Novais, M. S. Ding, M. S. Ferreira, S. Koch, S. Passerini, and J. L. Pinto, "Internal strain and temperature discrimination with optical fiber hybrid sensors in Li-ion batteries." *J. Power Sources*, **410**, 1 (2019).

33. S. Novais et al., "Internal and external temperature monitoring of a Li-ion battery with fiber bragg grating sensors." *Sensors*, **16**, 1394 (2016).

34. Y. Yu, T. Vincent, J. Sansom, D. Greenwood, and J. Marco, "Distributed internal thermal monitoring of lithium ion batteries with fibre sensors." *Journal of Energy Storage*, **50**, 104291 (2022).

35. C. Gervillié-Mouravieff, L. Albero Blanquer, C. Alphen, J. Huang, and J-M. Tarascon, "Unraveling SEI formation and cycling behavior of commercial Ni-rich NMC Li-ion cells through operando optical characterization." *J. Power Sources*, **580**, 233268 (2023).

36. L. Albero Blanquer, F. Marchini, J. R. Seitz, N. Daher, F. Bétermier, J. Huang, C. Gervillié, and J-M. Tarascon, "Optical sensors for operando stress monitoring in lithium-based batteries containing solid-state or liquid electrolytes." *Nat. Commun.*, **13**, 1153 (2022).

37. J. Bonefacino et al., "High-fidelity strain and temperature measurements of Li-ion batteries using polymer optical fiber sensors." *J. Electrochem. Soc.*, **169**, 100508 (2022).

38. K. M. Alcock, M. Grammel, Á. González-Vila, L. Binetti, K. Goh, and L. S. M. Alwis, "An accessible method of embedding fibre optic sensors on lithium-ion battery surface for in situ thermal monitoring." *Sens. Actuators, A*, **332**, 113061 (2021).

39. A. Raghavan et al., "Embedded fiber-optic sensing for accurate internal monitoring of cell state in advanced battery management systems part 1: cell embedding method and performance." *J. Power Sources*, **341**, 466 (2017).

40. C. Wang, Y. Wang, C. Cheng, Y. Hu, Y. Liu, and F. Yao, "Estimation of Li-ion battery SOH based on factors combination of FBG wavelength shift and charge-discharge process." *Infrared Phys. Technol.*, **140**, 105414 (2024).

41. M. Nascimento, T. Paixão, M. S. Ferreira, and J. L. Pinto, "Thermal mapping of a lithium polymer batteries pack with FBGs network." *Batteries*, **4**, 67 (2018).

42. J. Peng, S. Jia, H. Yu, X. Kang, S. Yang, and S. Xu, "Design and experiment of FBG sensors for temperature monitoring on external electrode of lithium-ion batteries." *IEEE Sens. J.*, **21**, 4628 (2021).

43. K. M. Alcock, Á. González-Vila, M. Beg, F. Vedreño-Santos, Z. Cai, L. S. M. Alwis, and K. Goh, "Individual cell-level temperature monitoring of a lithium-ion battery pack." *Sensors*, **23**, 4306 (2023).

44. L. W. Sommer, A. Raghavan, P. Kiesel, B. Saha, J. Schwartz, A. Lochbaum, A. Ganguli, C-J. Bae, and M. Alamgir, "Monitoring of intercalation stages in lithium-ion cells over charge-discharge cycles with fiber optic sensors." *J. Electrochem. Soc.*, **162**, A2664 (2015).

45. A. Ganguli et al., "Embedded fiber-optic sensing for accurate internal monitoring of cell state in advanced battery management systems part 2: Internal cell signals and utility for state estimation." *J. Power Sources*, **341**, 474 (2017).

46. Y. J. Ee, K. S. Tey, K. S. Lim, P. Shrivastava, S. B. R. S. Adnan, and H. Ahmad, "Lithium-ion battery state of charge (SoC) estimation with non-electrical parameter using uniform fiber bragg grating (FBG)." *Journal of Energy Storage*, **40**, 1 (2021).

47. O. Frazão, L. A. Ferreira, F. M. Araújo, and J. L. Santos, "Simultaneous measurement of strain and temperature using fibre Bragg gratings in a twisted configuration." *J. Opt. A: Pure Appl. Opt.*, **7**, 427 (2005).

48. C. J. Bae, A. Manandhar, P. Kiesel, and A. Raghavan, "Monitoring the strain evolution of lithium-ion battery electrodes using an optical fiber bragg grating sensor." *Energy Technology*, **4**, 851 (2016).

49. R. Kashyap, *Fiber Bragg Gratings* ()()(Academic Press)(, Burlington, MA) 4309 (2010).

50. K. O. Hill and G. Meltz, "Fiber Bragg grating technology fundamentals and overview." *J. Lightwave Technol.*, **15**, 1263 (1997).

51. A. Smith, P. Stüble, L. Leuthner, A. Hofmann, F. Jeschull, and L. Mereacre, "Potential and limitations of research battery cell types for electrochemical data acquisition." *Batteries & Supercaps*, **6**, e202300080 (2023).

52. K-Y. Oh et al., "Rate dependence of swelling in lithium-ion cells." *J. Power Sources*, **267**, 197 (2014).

53. K-Y. Oh and B. I. Epureanu, "A novel thermal swelling model for a rechargeable lithium-ion battery cell." *J. Power Sources*, **303**, 86 (2016).

54. P. Nazari, R. Bäuerle, J. Zimmermann, C. Melzer, C. Schwab, A. Smith, W. Kowalsky, J. Aghassi-Hagmann, G. Hernandez-Sosa, and U. Lemmer, "Piezoresistive free-standing microfiber strain sensor for high-resolution battery thickness monitoring." *Adv. Mater.*, **35**, 2212189 (2023).

55. R. J. Van Steenkiste and G. S. Springer, *Strain and Temperature Measurement with Fiber Optic Sensors* (Technomic Publishing, PA) (1996).

56. F. M. Kindermann, A. Noel, S. V. Erhard, and A. Jossen, "Long-term equalization effects in Li-ion batteries due to local state of charge inhomogeneities and their impact on impedance measurements." *Electrochim. Acta*, **185**, 107 (2015).

57. L. W. Sommer, P. Kiesel, A. Ganguli, A. Lochbaum, B. Saha, J. Schwartz, C-J. Bae, M. Alamgir, and A. Raghavan, "Fast and slow ion diffusion processes in lithium ion pouch cells during cycling observed with fiber optic strain sensors." *J. Power Sources*, **296**, 46 (2015).

58. X. Wang, Y. Sone, and S. Kuwajima, "In situ investigation of the volume change in Li-ion cell with charging and discharging." *J. Electrochem. Soc.*, **151**, A273 (2004).

59. X. Wang, Y. Sone, G. Segami, H. Naito, C. Yamada, and K. Kibe, "Understanding volume change in lithium-ion cells during charging and discharging using in situ measurements." *J. Electrochem. Soc.*, **154**, A14 (2007).

60. Z. Li, J. Zhang, B. Wu, J. Huang, Z. Nie, Y. Sun, F. An, and N. Wu, "Examining temporal and spatial variations of internal temperature in large-format laminated battery with embedded thermocouples." *J. Power Sources*, **241**, 536 (2013).

61. M. Li, W. Chen, Z. Shen, Z. Wang, Z. Ming, C. Wang, H. Tian, T. Sang, and R. Song, "Characterization of temperature and strain changes in lithium-ion batteries based on a hinged differential lever sensitization fiber bragg grating strain–temperature simultaneous-measurement sensor." *Sensors*, **24**, 412 (2024).

62. M. P. Mercer, C. Peng, C. Soares, H. E. Hoster, and D. Kramer, "Voltage hysteresis during lithiation/delithiation of graphite associated with meta-stable carbon stackings." *J. Mater. Chem. A*, **9**, 492 (2021).

63. Corning® SMF-28TM Optical Fiber Product Information, (2001).

64. A. J. Louli, L. D. Ellis, and J. R. Dahn, "Operando pressure measurements reveal solid electrolyte interphase growth to rank Li-ion cell performance." *Joule*, **3**, 745 (2019).